Catalysis Science & Technology

rsc.li/catalysis

ROYAL SOCIETY
OF **CHEMISTRY**
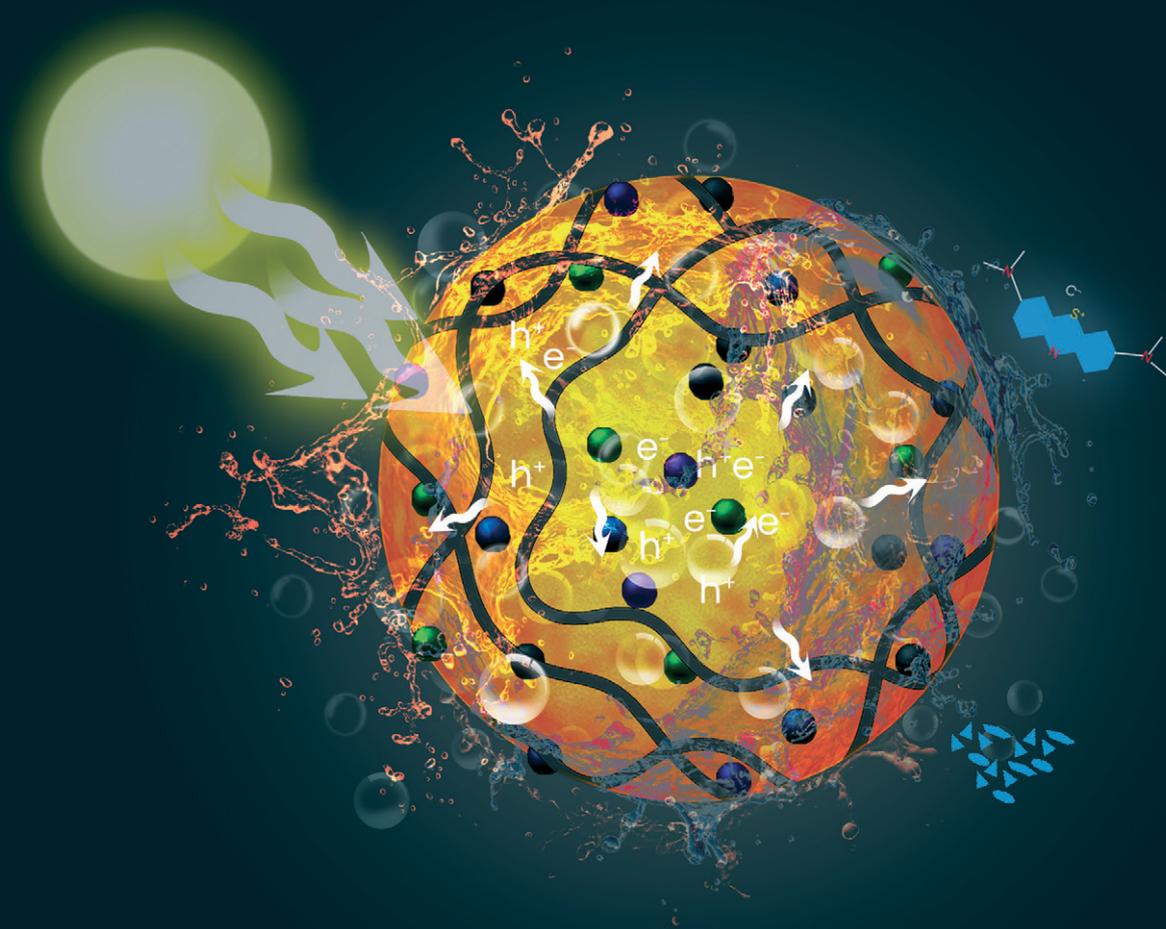
PAPER
Edith Mawunya Kutorglo *et al.*
Water-soluble polymers stabilize defects in a new
peroxo-titania: visible light-active γ-TiO$_2$ for photocatalytic
pollutant degradation and hydrogen production

ROYAL SOCIETY OF CHEMISTRY

PAPER

Check for updates

Water-soluble polymers stabilize defects in a new peroxo-titania: visible light-active y-TiO$_2$ for photocatalytic pollutant degradation and hydrogen production

Edith Mawunya Kutorglo, [iD] *[ac] Jan Šmahlík,[a] Yusef Hassan,[a] Minoo Tasbihi, [iD] [b] Pavel Sialini,[d] Wiebke Riedel, [iD] [e] Andrey Prokhorov, [iD] [fg] Eliška Zmeškalová, [iD] [ah] Kousik Das, [iD] [i] Reinhard Schomäcker, [iD] [b] Miroslav Šoóš[a] and Michael Schwarze[b]

The introduction of defects into photocatalyst materials has attracted current research attention because of the critical role that defects play in enhancing light absorption, charge transfer and interfacial reactions. However, the harsh synthesis conditions and the instability of surface defects in air lead to the loss of reactive interface sites. Therefore, the sustainable development of stable, defect-rich photocatalysts remains a significant challenge. In this work, we discovered that water-soluble polymeric dispersants stabilize defects in a new peroxo-TiO$_2$ exhibiting four different titanium valence states, Ti^{4+}, Ti^{3+}, Ti^{2+} and Ti^0, which has not yet been reported. The multiple oxidation states of Ti is due to the generation of titanium vacancies in y-TiO$_2$, resulting in a low bandgap of 2.42 eV, high surface area and photocatalytic activity for hydrogen production and pollutant degradation. The calcined y-TiO$_2$ with 1% deposited Pt achieved a remarkably high H$_2$ production (1.65 mmol g^{-1} h^{-1}), which is nearly 20 times as high as that of the pristine, as-prepared yellow TiO$_2$ (y-TiO$_2$, 0.082 mmol g^{-1} h^{-1}) under solar-simulated irradiation. This value far exceeds the hydrogen production of similar defect-rich catalyst materials reported so far when sunlight is used as an irradiation source. The y-TiO$_2$ catalyst particles were immobilized onto a plate and into alginate films and beads, which readily adsorbed and degraded methylene blue dye. The plates, films and beads were regenerated multiple times under solar simulation. Thus, this strategy of using water-soluble polymers to synthesize stable defects in photocatalysts offers new insights into solving the issue of defect instability in catalytic materials.

Introduction

The recent interest in combining free sunlight with semiconductor catalysts for tackling current environmental

[a] Department of Chemical Engineering, University of Chemistry and Technology Prague, 166 28 Prague, Czech Republic. E-mail: kutorgle@vscht.cz

[b] Department of Chemistry, Technische Universität Berlin, 10623 Berlin, Germany

[c] Department of Immunology, NMIMR, College of Health Sciences, University of Ghana, Accra, Ghana

[d] Central Laboratories, University of Chemistry and Technology Prague, 166 28 Prague, Czech Republic

[e] Institut für Chemie und Biochemie, Freie Universiät Berlin, 14195, Berlin, Germany

[f] Institute of Physics AS CR, Na Slovance 2, 18221 Prague, Czech Republic

[g] Institute of Plasma Physics of the Czech Academy of Sciences, 182 00, Prague, Czech Republic

[h] Department of Structure Analysis, Institute of Physics of the Czech Academy of Sciences, Czech Republic

[i] Department of Chemistry, Metalorganics and Inorganic Materials, Technische Universität Berlin, Berlin 10623, Germany

and energy-related problems has opened new opportunities for sunlight-driven redox reactions. Examples include CO$_2$ reduction to chemicals and fuels, organic pollutant degradation, hydrogen production from water, α-oxygenation of amides and H$_2$O$_2$ production, among others.[1–6] Unfortunately, the majority of the conventional photocatalysts, *e.g.* TiO$_2$, exhibit several inherent drawbacks such as low surface areas, low sunlight absorption due to large bandgaps, and rapid charge recombination,[7–10] resulting in inefficient light absorption, low adsorption capacities and catalytic efficiencies.[11,12]

In recent years, defect-rich photocatalysts have emerged with a great potential because of the critical role that defects play in light absorption, charge separation and transfer as well as interfacial reactions.[7,12–15] These materials usually exhibit narrow bandgaps, which extend their light absorption into the visible and near-infrared (NIR) regions.[12,16,17] For instance, Wu and co-workers[18] prepared ultra-small yellow defective TiO$_2$ by a UV-light-assisted sol–gel method, which

5986 | *Catal. Sci. Technol.*, 2025, **15**, 5986–6000

This journal is © The Royal Society of Chemistry 2025

showed 3.7-fold increase in hydrogen production compared to the normal TiO$_2$. Similarly, other defective materials including yellow TiO$_2$,[19] black TiO$_2$,[20,21] blue TiO$_2$,[22–25] and TiO$_2$-based composites[15,26,27] have been developed and found to have the ability to catalyse reactions in various fields. In addition, defects are known to serve as active sites where catalytic reactions occur, consequently resulting in enhanced photocatalytic performance.[9]

Unfortunately, preparing stable defects with the desired properties is challenging and the preparation methods for most of these defect-rich materials are harsh and expensive, often requiring high temperatures (>200 °C) and pressures or vacuum, plasma etching, long synthesis times, and the use of fluorine salts, which are toxic and contaminative.[9,13,28] In addition, the majority of the resulting materials also suffer from low surface areas.[12] The biggest challenge, however, for these defect-rich TiO$_2$ materials is that the surface defects are highly unstable in air and re-oxidation readily occurs upon exposure to oxygen, resulting in loss of photocatalytic performance. Taking the ultra-small yellow defective TiO$_2$ as an example, Wu et al.[18] did not observe any obvious peak for Ti^{3+} defects in the XPS spectra of ultra-small yellow defective TiO$_2$, which was prepared by a UV-light-assisted sol–gel method. The authors attributed this to the fact that the photo-induced Ti^{3+} was quickly oxidized back to Ti^{4+} by the oxygen present in the air after the UV light was turned off. Fan Zuo et al. (2010)[29] and Chengyu Mao et al. (2014)[30] made similar observations that there was no evidence of Ti^{3+} species in the self-doped Ti^{3+} as measured by XPS. This was attributed to the fact that the surface Ti^{3+} groups are not stable enough in air and are susceptible to oxidation by dissolved oxygen in water. In addition to this challenge of instability of defects, there are very few reports on these defect-rich yellow titania photocatalysts and the ambiguity relating to the contribution of these defects towards improving light absorption and photocatalytic performance.[16,31,32] Therefore, the development of simpler methods for designing photocatalysts with stable defects and understanding their formation mechanisms still remains a stimulating topic.

In this work, we report a new strategy to develop a stable, defect-rich peroxo-TiO$_2$ (named yellow TiO$_2$ because of its deep yellow colour and shortened as y-TiO$_2$) by performing the synthesis in the presence of water-soluble polymeric stabilizers to form stable Ti–O and Ti–OH groups on the surface. This y-TiO$_2$ catalyst is characterized by four different valence states of titania, Ti^{4+}, Ti^{3+}, Ti^{2+} and Ti^0, which has not yet been reported. The material exhibited a low bandgap, enhanced absorption in the visible region and a highly mesoporous structure. By irradiating the materials under solar simulation, high photocatalytic activity was demonstrated for hydrogen production from aqueous methanol solution as well as organic pollutant degradation. Thus, this work provides a robust, environmentally friendly approach for the design of stable, defect-rich photocatalysts with improved performance for solar-driven applications.

Experimental part

All chemicals used were of analytical grade and used without any modification or purification (more details in the SI).

Catalyst synthesis

Synthesis of stable, defect-rich y-TiO$_2$ catalyst. The y-TiO$_2$ catalysts were prepared using a simple and environmentally friendly approach which combined a sol–gel method via hydrolysis of titanium(IV) isopropoxide (TTIP) and a colloidal approach using PVA or PVP as a stabilizer. First, 100 mg of PVA was dissolved in 100 mL of distilled water at 85 °C in a 3-neck flask equipped with a condenser and a thermometer for monitoring the temperature. After complete dissolution of PVA, the heating was turned off and the solution was kept under stirring. Into a separate flask, 30 mL of methanol was added, then 10 mL of TTIP was added dropwise into the methanol and the mixture was stirred for 5–10 minutes (solution A). After cooling of the PVA solution to about 75 °C, an H$_2$O$_2$/H$_2$0 solution (10 mL of 30% H$_2$O$_2$ and 10 mL of DI water) was added. The mixture was stirred for about 10 minutes (solution B). The temperature was around 70 °C at this point. The methanol/TTIP mixture (solution A) was added dropwise into the PVA/H$_2$O$_2$ solution (solution B) in the 3-neck round bottom flask while stirring. The addition of solution A to B when done too quickly generates heat and a huge amount of foam, thus this step needs to be done very slowly and under constant stirring. About 50 mL of DI water was used to rinse the flasks and added to the mixture in the 3-neck flask. Then 1.5 mL of NH$_4$OH solution was added to the reaction mixture to adjust the pH to around 9. The reaction mixture was heated up to 85 °C again. When the temperature reached 85 °C, the reaction was left to run for 1 h, resulting in a yellow gelatinous solution. After 1 h of reaction, the flask was lifted out of the heating mantle and left in the fume hood to cool. The cooled solution was centrifuged at 10 000 rpm and 25 °C for 10 minutes using a refrigerated benchtop centrifuge (Thermo Scientific Heraus Multifuge X3R by Thermo Electron LED GmbH, Germany) and the particles were washed with distilled water several times until the supernatant was clear. Finally, the obtained yellow solid was dried in a vacuum oven at 60 °C for 24 h. The resulting y-TiO$_2$ particles were ground using a mortar and pestle and stored for further use. A white mesoporous TiO$_2$ catalyst was synthesized following a similar approach as detailed in Text S2 in the SI. Calcination was performed in air at 550 °C to produce the highly crystalline mesoporous catalysts. The temperature was increased at a rate of 5 °C min^{-1} from room temperature to the desired temperature and held there for 3 h.

Catalyst characterization

A combination of analytical techniques was employed to characterize the physicochemical properties of the prepared materials as detailed in Text S3 in the SI. Briefly, the

This journal is © The Royal Society of Chemistry 2025

Catal. Sci. Technol., 2025, 15, 5986–6000 | 5987

morphology and structure were observed under a field emission scanning electron microscope (FESEM) and transmission electron microscope (TEM), respectively. An X-ray powder diffractometer (XRD) was employed to investigate the crystalline structure, whereas the functional groups in the prepared materials were identified by Fourier-transform infrared (FTIR) spectroscopy. The surface functional groups were characterized using an X-ray photoelectron spectroscope (XPS, Omicron Nanotechnology) with a monochromatic Al Kα radiation source (E = 1486.7 eV) working at 12 kV, E_{pass} = 40 eV, with a 0.2 eV energy step in constant analyzer energy (CAE) mode. UV-vis absorbance (on particles in solution) and UV-DRS measurements (on solid powder catalysts) were conducted using a Perkin Elmer Lambda 35 UV/vis spectrometer between 200 and 800 nm. BET surface areas were determined from N_2 adsorption–desorption isotherms measured at 77 K, with samples degassed at 150 °C for 2–4 h prior to measurements. The pH point of zero charge (PZC) was estimated by dispersing the particles in water with pH adjusted from 3 to 11. Continuous wave (cw) electron paramagnetic resonance (EPR) measurements at X-band (9.45 GHz) frequencies were conducted at 110 K with a Bruker B-ER420 spectrometer upgraded with a Bruker ECS 041XG microwave bridge and a lock-in amplifier (Bruker ER023M) to further evaluate the defects in y-TiO₂. Photocurrent responses were recorded using a three-electrode electrochemical setup, comprising the sample-deposited FTO as the working electrode, a platinum wire as the counter electrode, and an Ag/AgCl electrode as the reference electrode. A 0.5 M Na_2SO_4 aqueous solution served as the electrolyte. Illumination was provided by a 300 W xenon lamp equipped with a solar light filter. The Ag/AgCl reference electrode was pre-calibrated in the same electrolyte against the reversible hydrogen electrode (RHE), and all potentials reported herein are converted and referenced to the RHE.

Catalyst performance testing

To investigate the photocatalytic activity of the prepared y-TiO₂ materials, hydrogen production and organic pollutant degradation under simulated sunlight irradiation were tested.

1Hydrogen production: for the hydrogen production test, 20 mg of the catalyst was loaded into a 250 mL glass photoreactor with a top irradiation window fitted with quartz glass (Fig. S1 in the SI). About 40 mL of 10 vol% aqueous ethanol solution was added into the reactor and 20 μL of hexachloroplatinic(ɪv) acid hydrate was added. The suspended catalyst particles were continuously stirred throughout the course of the reaction using a magnetic stirrer. The reactor was closed with septum fitted caps and the suspension was degassed by purging the headspace with high-purity argon for 30 minutes. A solar simulator (L.O.T. Oriel Quantum Design, Germany) equipped with an AM 1.5 filter was used to irradiate the

reaction mixture which was kept under constant stirring for 5 h. Reproducibility was ensured by repeating the test one more time under the same conditions. The amount of evolved gas was analysed by a gas chromatograph (GC Agilent 7890 A) equipped with a thermal conductivity detector (TCD) and evaluated using a previously prepared calibration plot. The hydrogen produced (mmol) was calculated using eqn (1) and later converted to the rate of H₂ gas production:

$$H_2 \text{ produced} = \frac{H_2 \text{ (detected by the GC)}}{V_m \text{ (H}_2\text{)}} \times V_{Headspace} \quad (1)$$

V_m (H₂) = 24.5 L mol⁻¹ is the molar volume of hydrogen at 25 °C. $V_{Headspace}$ is the volume of the reactor headspace = 210 mL.

Organic pollutant adsorption and degradation. As an alternative application, we tested the adsorption and photocatalytic degradation of methylene blue (MB), a model thiazine cationic dye in batch mode. In a typical photocatalytic adsorption–degradation reaction, about 20 mg of the y-TiO₂ catalyst was mixed with 40 mL of MB solution (25 mg L⁻¹ and catalyst dose = 0.5 g L⁻¹) under continuous stirring. The reaction mixture was either left in the dark (to prevent photocatalysis and photolysis during the dye adsorption step) or irradiated using a solar simulator (AM 1.5 filter from L.O.T. Oriel Quantum Design, Germany) under stirring (for simultaneous adsorption–degradation). The dye adsorption performance of the prepared materials was compared with that of commercial TiO₂ P25. The dye concentration was monitored with a UV-vis spectrophotometer, where about 2 mL of the dye solution was collected from each sample after 30 minutes. The nanoparticles were separated by filtering through a 0.45 μm PTFE syringe filter and the particle-free solution was measured. Thereafter, subsequent samples were collected at 1-h intervals for up to 5 h. The residual dye concentrations were estimated from the absorbance values measured at the λ_{max} of the dye using calibration curves (Fig. SI 2 in the SI) to evaluate the decolorization efficiency and degradation kinetics. The amount of dye adsorbed and the dye removal efficiency (R) as well as the adsorption capacity at equilibrium (q_e, mg g⁻¹) and different time intervals (q_t, mg g⁻¹) were calculated. In addition, three established adsorption models (Langmuir, Freundlich and Temkin) were employed to investigate the adsorption behavior of the MB dye onto the peroxo-TiO₂ and the binding parameters were evaluated.

For the kinetic adsorption tests, 20 mg of the y-TiO₂ NPs was added into 40 mL of 25 mg L⁻¹ MB solution and the dye concentration at different time intervals (every 30 minutes) was measured. The kinetic data were fitted using pseudo-first-order (2) and pseudo-second-order (3) equations according to the following models:

$$\text{Pseudo-first-order} \quad \ln(q_e - q_t) = \ln q_e - k_1 t \quad (2)$$

5988 | *Catal. Sci. Technol.*, 2025, **15**, 5986–6000

This journal is © The Royal Society of Chemistry 2025

$$\text{Pseudo-second-order} \quad \frac{t}{q_t} = \frac{1}{k_2 q_e^2} + \frac{t}{q_e} \qquad (3)$$

Practical considerations: ease of handling and reusability

To facilitate easy handling of the catalysts, the as-prepared y-TiO_2 catalyst powder was deposited on a metal plate or incorporated into sodium alginate beads or films.

Deposition of the catalyst particles on a plate: the deposition of y-TiO_2 catalyst powder was done *via* a layer-by-layer deposition approach using silica binder to improve the adhesion strength of the particles. First, 50.35 mg of the y-TiO_2 powder was weighed into a vial and 350 μL of silica binder and 1.25 mL of 1-propanol were added. The mixture was stirred for about 5 minutes and then sonicated for 10 minutes. The mixture was applied onto the metal plate using a brush one layer at a time, followed by drying at 60 °C for about 1–3 minutes. This was repeated for the next layers until the entire mixture was applied. The films were then dried at 60 °C for 3 h.

Encapsulation of y-TiO_2 catalyst into sodium alginate beads and films: first, sodium alginate solution (2 wt%) was prepared by dissolving sodium alginate in water. Then, about 50–100 mg of y-TiO_2 was dispersed in the 2 wt% sodium alginate solution before proceeding to step 3 to form either beads or films. In a separate flask, 100 mL of 4–5 wt% $CaCl_2$ solution was prepared and poured into a crystallization dish. The sodium alginate/y-TiO_2 mixture (100 μL) was dropped into the $CaCl_2$ solution using a pipette to form the beads with encapsulated y-TiO_2 catalysts or poured into a watch glass and immersed into the $CaCl_2$ solution. The encapsulated catalyst beads or films were separated from the $CaCl_2$ solution and washed with distilled water several times. The films, beads, and plate with immobilized particles were tested in the dye adsorption–photocatalytic degradation tests.

Photocatalytic degradation and reuse of the y-TiO_2 beads, films and plates. The reusability of the immobilized particle on a plate was systematically investigated in five repeated adsorption–degradation cycles by irradiation of the dye-adsorbed plate under solar simulation. First, the plate was immersed into the dye solution to allow enough time for adsorption. After each adsorption cycle, the immobilized particles with adsorbed MB were removed from the solution, placed in a Petri dish with distilled water and irradiated for about 1 h with a solar simulator to degrade the dye so the plate can be available for further reusing in the next cycle. The degradation efficiency was determined by measuring the MB adsorption in the next adsorption cycle and comparing the value with the previous measurement.

Results and discussion

Defect-rich y-TiO_2 catalyst development and performance testing

The defect-rich, y-TiO_2 catalyst with highly mesoporous structure was prepared *via* a simple approach, which combines a sol–gel technique through the hydrolysis of
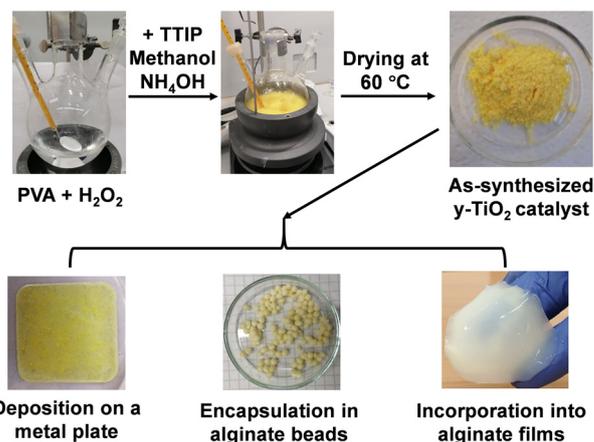

Fig. 1 Synthesis approach to the development of defect-rich y-TiO_2 and its deposition onto a plate and incorporation into beads or films.

titanium(IV) isopropoxide (TTIP) and a colloidal method in the presence of water-soluble polymeric stabilizers, *i.e.* polyvinyl alcohol (PVA) and polyvinylpyrrolidone (PVP) (Fig. 1). Subsequently, the organic pollutant degradation and the hydrogen production performance of the as-prepared and calcined y-TiO_2 catalysts were evaluated under irradiation with a solar simulator. A combination of analytical techniques was employed to confirm the formation of the amorphous peroxo-TiO_2, which comprises the following surface oxygen groups: Ti–O, Ti–OH, –C=O, –C–O– and O(B) (see XPS results in Fig. S9).

The role and mechanism of water-soluble stabilizers in defect stabilization

Defects present in photocatalysts such as oxygen vacancies and surface hydroxyl groups, among others, do not only act as active sites for photocatalytic reactions. They can also improve charge separation by trapping charge carriers and modify band structures to enhance visible light absorption. Unfortunately, most of these defects are unstable and undergo fast recombination, limiting their use during reactions. In this study, we employed poly(vinyl alcohol) (PVA) as a flexible, water-soluble polymer for modulating the surface charges and chemistry to stabilize Ti^{3+} defects and oxygen vacancies in peroxo-titania and improve visible light photocatalysis. Based on the results obtained from the different material characterizations, a reaction mechanism for the stabilization of defects in the y-TiO_2 by the water-soluble polymeric stabilizers is proposed to involve the interaction of the stabilizer with defect sites preventing them from recombining and cross-linking of the stabilizer and surface defects in peroxo-titania through hydrogen and covalent bonding stabilizing the local environment around the defects.[33–35] Specifically, valence-unfilled Ti(IV) ion centers and O(II) are known to exist which form basic ≡TiOH and acidic ≡OH, respectively, on the TiO_2 surface in aqueous solution. When H_2O_2 is added during the synthesis of y-TiO_2,

This journal is © The Royal Society of Chemistry 2025

Catal. Sci. Technol., 2025, **15**, 5986–6000 | **5989**

the –OOH groups of H_2O_2 substitute for the OH groups in the basic $\equiv$TiOH to form a yellow surface complex, the so-called peroxo-TiO_2 complex (Ti–O– O–Ti).[36,37] In the y-TiO_2 material, there are abundant peroxo groups (–O–O–), which change the chemical bonding orientation of Ti–O and the crystalline properties and surface groups. This complex is highly reactive due to the presence of peroxide groups. In the presence of PVA, the hydroxyl groups (–OH) in PVA interact with the peroxo groups in the peroxo-TiO_2 complex, leading to the formation of hydrogen bonds and possibly covalent bonds between PVA and TiO_2, resulting in cross-linking, where multiple PVA chains are linked together through TiO_2. This cross-linking enhances the mechanical properties and stability of the resulting peroxo-TiO_2 composite material. Based on these interactions, the role of the water-soluble polymer (PVA) is revealed to be dual: inducing the formation of different valence states and stabilization of the peroxo complex. Ti exhibits sixfold coordination in anatase and rutile phases, but the presence of PVA with multiple hydroxyl groups in the reaction medium interferes with the formation of the pure Ti phase, resulting in different Ti states with oxygen vacancies. The electrons in the vacancy at the interface of TiO_2 and PVA move toward the neighboring Ti atoms, creating reduced Ti^{3+} and Ti^{2+} cations.[38] The polymer chains of PVA also form a protective layer on the surface of the particles, limiting the diffusion of oxidants into the Ti^{3+}-rich surface and helping to preserve the defects and oxygen vacancies.[33] Overall, the main role that the water-soluble polymers play in the stabilization of defects is *via* the binding through –OH groups of PVA and the Ti^{3+}/Ti^{4+} peroxo groups forming crosslinks *via* hydrogen bonding and covalent interactions, passivating the surface around the defects, which stabilizes the peroxo-TiO_2 material for use over repeated photocatalytic cycles.

Photocatalytic hydrogen evolution

The H_2 production rate of the as-prepared y-TiO_2 prior to any calcination treatment was low, 82 µmol g^{-1} h^{-1}, which indicates that the as-prepared y-TiO_2 could not catalyze H_2 production efficiently (Fig. 2A). This could be due to the highly amorphous nature of the peroxo groups, which made the entire material less crystalline. Nevertheless, it is still noteworthy that the as-prepared material even with no prior treatment or without addition of any noble metal co-catalyst produced some hydrogen under solar-simulated irradiation. This could be attributed to the highly mesoporous structure which provides a shorter distance for the electron–hole pairs to reach the photocatalyst surface as well as the improved light absorption. No hydrogen was generated in the absence of the photocatalyst or in the dark (no irradiation). When y-TiO_2 was calcined, the hydrogen production rate increased about three times to 255 µmol g^{-1} h^{-1}, implying that the calcined y-TiO_2 possessed enhanced catalytic activity which could be due to an improvement in the crystalline properties and the
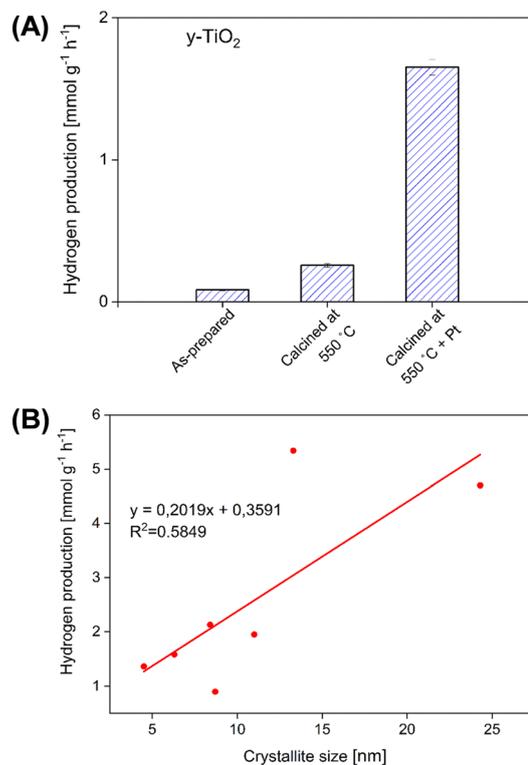

Fig. 2 (A) Hydrogen production rate of the prepared y-TiO_2 catalysts and (B) relationship between crystalline size and hydrogen production.

introduction of active catalytic sites. This is the first report of such a defect-rich TiO_2 which is highly mesoporous (S_{BET} = >380 m^2 g^{-1}), exhibits a high negative surface charge due to the generation of –C–O–, Ti–O and Ti–OH– groups and has a high solar photocatalytic activity. Interestingly, under the studied conditions, the calcined y-TiO_2 could steadily produce high amounts of hydrogen gas at a rate of 1.65 mmol g^{-1} h^{-1} from aqueous ethanol solution when Pt was deposited as a co-catalyst. The increased H_2 production after the addition of the co-catalyst is due to the fact that Pt efficiently traps photogenerated electrons that migrate to the surface of y-TiO_2, thereby facilitating charge separation, which is in line with previous reports.[39–41] Because no decrease in the H_2 production rate was observed during the irradiation step for about 5 to 8 h, we confirmed that the catalysts were photostable. From previous reports, the value of hydrogen production of y-TiO_2 catalyst is significantly higher than those of defect-rich TiO_2-based catalysts irradiated under a solar simulator (see Table 1). However, the performance is lower compared to that of the TiO_2-based catalysts tested under ultraviolet (UV) light irradiation.[40,42–45]

Even though it is obvious that the catalysts irradiated under UV light typically have better performances compared to those performed under solar simulator irradiation, still, a one-to-one comparison cannot be made because of other factors which might affect the photocatalytic process such as the type and concentration of sacrificial agent used, the

5990 | *Catal. Sci. Technol.*, 2025, **15**, 5986–6000

This journal is © The Royal Society of Chemistry 2025

Table 1 Comparison of TiO$_2$-based photocatalysts for H$_2$ production reported in the literature

Catalyst/Co-catalyst	Irradiation conditions	H$_2$ production [mmol g^{-1} h^{-1}]	Ref.
1. Cu–TiO$_2$	300 W Xe lamp	21.05	42
2. Au–Pd/TiO$_2$	100 W ultraviolet lamp	12.00	40
3. 0.4Ni2P/TiNR	300 W Xe lamp	9.38	46
4. Pt–Pd SAs/Vo–TiO$_2$	300 W Xe lamp	4.24	47
5. TiO$_2$/Au 1.5	Solarium Philips HB 175 lamps, each equipped with 4 × 15 W Philips CLEO fluorescent tubes, 300 to 400 nm (max. at 365 nm)	1.118 (μmol h^{-1})	48
6. TiO$_2$-M-6, aerogel	Ultraviolet (UV) light, 300 W Xe lamp with a light filter ranging 240 to 400 nm	0.0975	44
7. 2.5% RGO-TiO$_2$ NT	300 W Xe lamp (Excelitas, PE300BFM)	>4.00	45
8. TiO$_2$-RGO	300 W Xe/mercury lamp	1.13	43
9. TiO$_2$ aerogel (Pt)	300 W Xe lamp (cutoff filter 410 nm)	0.328	49
10. Black TiO$_2$/Pt 1%	300 W Xe lamp (cutoff filter 410 nm)	0.1384	50
11. B/Rh$_{0.5}$–TiO$_2$	Xe lamp with an AM 1.5G filter or a 420 nm cutoff filter	Approx. 17.00	51
12. Y-TiO$_2$ calcined/Pt	300 W Xe arc lamp with an AM 1.5G filter	1.65	This study

amount and type of co-catalyst *etc.*[44] Thus the comparison of these results with previous studies only seeks to demonstrate the successful and efficient utilization of the simulated sunlight by the y-TiO$_2$ catalyst and to highlight the trend in performance. Evaluating the hydrogen production rate of a series of materials with various crystallite sizes and surface areas shows only a slight correlation between the hydrogen production and crystal sizes (Fig. 2B). This suggests that apart from the crystalline properties, the surface area, light absorption and pore sizes may also be important factors contributing to the enhanced performance of the catalyst. Consequently, it is believed that the high surface areas of the y-TiO$_2$ catalyst contributed to enhance diffusion and the rich surface defects enable access to active sites, thereby improving the photocatalytic performance.

Organic pollutant adsorption and photocatalytic degradation

Aside from hydrogen production over the y-TiO$_2$ catalyst, the high mesoporosity of the as-prepared catalyst coupled with the presence of surface functional groups makes it an excellent candidate for enhanced adsorption and photocatalytic degradation of organic pollutants. Despite the fact that adsorption is one of the most efficient and clean methods for removing contaminants from water, the surfaces of conventional adsorbents easily become saturated, often requiring costly regeneration or replacement. Therefore, catalysts exhibiting high surface areas, surface functional groups and solar photocatalytic activity are of special interest as they offer the possibility of simultaneous high adsorption and regeneration of the materials *via* solar photocatalysis.

Preliminary batch adsorption tests conducted with aqueous MB solution confirmed the good adsorption property of the as-prepared y-TiO$_2$. Because commercial TiO$_2$ P25 is the benchmark photocatalyst that has been intensively investigated, we selected TiO$_2$ P25 and calcined y-TiO$_2$ to test for dye adsorption and subsequent photocatalytic degradation. Interestingly, the as-prepared y-TiO$_2$ catalyst effectively adsorbed all the methylene blue dye molecules from water, with the catalyst particles settling at the bottom

of the bottle as a purple residue, leaving a clear solution on top (Fig. S3 in the SI). In contrast, it was observed that the dye adsorption of the calcined y-TiO$_2$ and even that of the commercial TiO$_2$ P25 were significantly lower, if not negligible, when compared to that of the as-prepared y-TiO$_2$ (Fig. S3 in the SI, b–d).

The adsorption isotherm measured using an initial MB concentration of 25 mg L^{-1} with varying doses of the y-TiO$_2$ catalyst (5 to 25 mg) revealed that the adsorption capacity increased with an increase in the amount of y-TiO$_2$ which also corresponded to a decrease in absorbance of the dye solutions (Fig. 3A). The fact that the adsorption process occurred fast at the beginning could be due to the high number of active sites available for adsorption as well as the enhanced surface area from the highly mesoporous structure.

As can be seen from Fig. 3 and S4 in the SI, when the y-TiO$_2$ catalyst amount reached 15 mg, the dye was fully removed. Thus, further addition of adsorbent beyond 15 mg was not necessary and the dose of y-TiO$_2$ was fixed to 15 mg for the subsequent experiments when using the same dye concentration. The equilibrium data were fitted with three types of well-established adsorption models, *i.e.* Langmuir, Freundlich and Temkin isotherm models (Fig. S5, SI). Overall, it was observed from the linear plot of C_e/q_e *vs.* C_e (Fig. 3B) that the correlation coefficient of the Langmuir plot is very high as compared to that of Freundlich and Temkin isotherms, confirming the suitability of this model to describe the adsorption behaviour onto y-TiO$_2$. Thus, these results suggest that the maximum adsorption on y-TiO$_2$ corresponds to a saturated single layer of solute on the adsorbent surface, with the adsorption capacity of the y-TiO$_2$ for methylene blue dye calculated to be 116 mg g^{-1}. Detailed description of the adsorption isotherms and optimization of adsorption parameters is presented in Text S4 and Fig. S6 in the SI.

To evaluate the adsorption kinetics, the MB solution concentration was analyzed at different times after the addition of the y-TiO$_2$ photocatalyst. The adsorption of MB onto y-TiO$_2$ proved to be relatively fast initially, with more than 50% of the dye adsorbed in just 30 minutes, and then
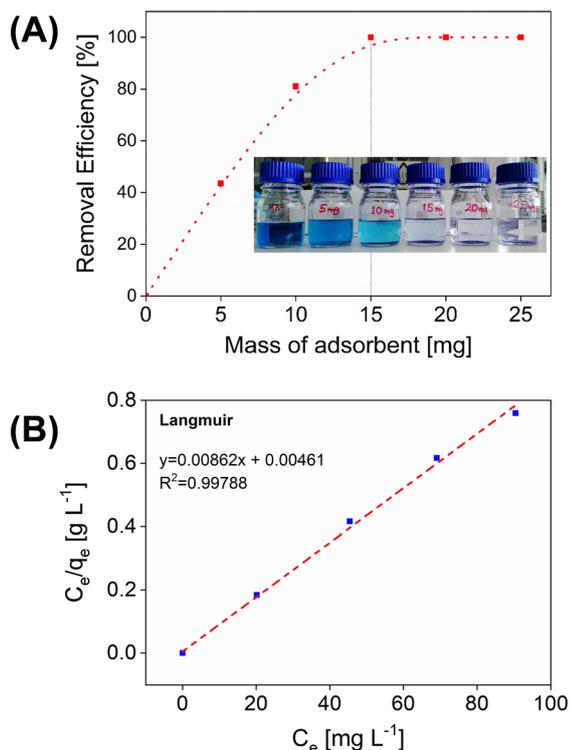
This journal is © The Royal Society of Chemistry 2025

Catal. Sci. Technol., 2025, **15**, 5986–6000 | **5991**

Fig. 3 (A) Effect of adsorbent dose (y-TiO$_2$ dosage) on the dye removal efficiency; concentration of MB solution = 25 mg L^{-1}, equilibration time = 24 h [inset shows photo of the adsorption]. (A) Adsorption isotherm of MB on y-TiO$_2$ fitted by the Langmuir model.

moved towards equilibrium after about 90 minutes (Fig. 4A, i). The rapid adsorption within the short contact time can be
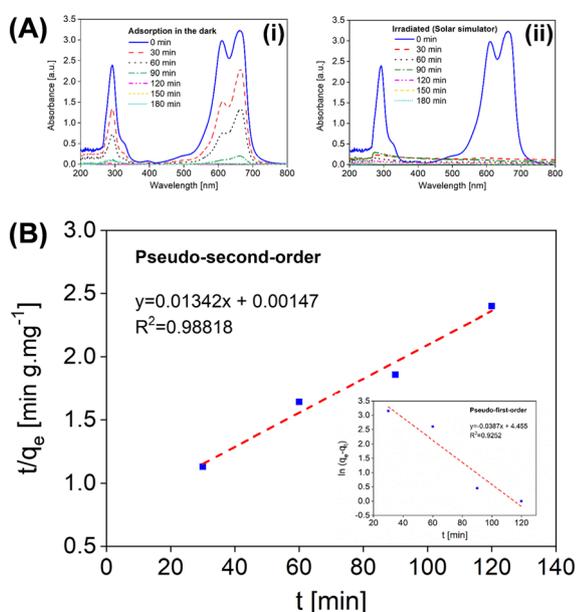

Fig. 4 (A) Kinetics of MB adsorption (i) in the dark and (ii) under solar simulation (initial dye concentration 25 mg L^{-1}, catalyst amount 0.5 g L^{-1}, volume of solution 40 mL). (B) Pseudo-second-order kinetic plot (inset is pseudo-first-order kinetic plot).

attributed to two main factors. First, the highly mesoporous nanostructure (average pore size of 10 nm) could facilitate fast diffusion of the MB molecules whose size is 1.43 nm. Secondly, the abundant oxygen-containing functional groups on the surface of y-TiO$_2$ provided vacant adsorption sites initially that enhanced its electrostatic interaction with the MB dye.

When the y-TiO$_2$/MB solution was irradiated with a solar simulator (combined adsorption and degradation), dye removal was very fast, reaching 100% removal in 30 minutes as obvious from the UV/Vis spectra (Fig. 4A, ii). This confirms the synergistic effect of high adsorption with photocatalytic degradation property. The resulting adsorption data were fitted using pseudo-first-order (plot of ln ($q_e - q_t$) vs. t) and pseudo-second-order (plot of t/q_t vs. t) kinetic models, which gave a linear relationship (Fig. 4B and S5 in the SI). The R^2 value obtained in the case of the pseudo-second-order kinetic plot was higher (0.98818) than that from the pseudo-first-order kinetic plot (0.9252). This suggests that the kinetics of MB adsorption on y-TiO$_2$ followed a pseudo-second-order model with electrostatic interactions on the surface being the rate-limiting step in the adsorption process.

In addition to the high adsorption capacity and fast kinetics, another advantage of the y-TiO$_2$ catalysts developed in this work lies in their simple regenerability under solar irradiation, without the need for any chemical additives. To ensure easy use and regeneration of the catalyst particles, immobilized catalysts prepared on plates, beads and in the form of a film (see Fig. 1), we demonstrated a two-step approach consisting of dye adsorption and subsequent photocatalytic dye degradation under the irradiation with a solar simulator. This stepwise approach was adopted because the adsorption process is rather slow and performing adsorption and photocatalytic degradation simultaneously is less effective. This is because it takes too long for the dye molecules to come in contact with the catalysts for the process to start. With this two-step adsorption–degradation approach, the dye molecules were first adsorbed onto the catalyst, close to the active sites and thus once irradiated, the degradation step proceeds faster. As illustrated in Fig. 5, the immobilized
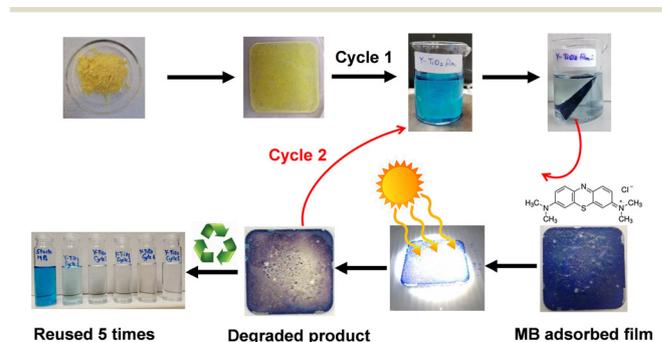

Fig. 5 Cycle of adsorption of methylene blue dye onto y-TiO$_2$ deposited plate and the solar-driven photocatalytic degradation of the dye, which led to regenerated film for use in 5 subsequent cycles.

5992 | *Catal. Sci. Technol.*, 2025, **15**, 5986–6000

This journal is © The Royal Society of Chemistry 2025

catalyst plate was immersed into the dye solution, and after the dye is adsorbed, the catalyst films were irradiated with a solar simulator for 1 h to initiate the photocatalytic degradation process of the MB dye. The regenerated films were reused (for 5 cycles) without significant loss in capacity compared with the blank film made without the catalyst, whose regeneration was not possible (Fig. S7c in the SI).

The regeneration was also applicable in the cases of the alginate beads and films (Fig. 6), which confirms the robustness of the catalyst immobilization or incorporation approaches for widespread practical application. Considering that both processes – H_2 production from aqueous methanol solution and the organic dye degradation – occurred under simulated sunlight irradiation, these results confirm the visible-light photocatalytic activity of the materials. The improved light absorption and high surface area enabled the solar light-driven photocatalytic performance of the particles. Considering the ease of preparation using safe precursors and the synergistic effect of high surface area and improved light absorption, the developed materials can be used in combination with the abundant energy from the sun to drive photocatalytic reactions.

Physical, chemical and thermal stability

The stability of the catalyst materials is crucial in enhancing their long-term performance and lowering costs. To evaluate the stability of the y-TiO$_2$ catalyst particles over multiple reaction cycles, a thin film of y-TiO$_2$ particles was prepared using PVA (enables easy separation and regeneration). This catalyst film was reused repeatedly for four repeated cycles for the photodegradation of MB dye to test whether the catalyst is stable and still active after multiple cycles. After each cycle, the films were washed with distilled water and irradiated using a solar simulator. A fresh batch of the 10 mg L^{-1} dye solution was added for the next cycle to be carried out under the same operating conditions. Fig. S13(c) shows that the photodegradation rate decreased only slightly in the second, third and fourth

cycles as compared to the first cycle. These results show that the y-TiO$_2$ catalyst is stable for the degradation of dyes under light irradiation. The slight loss in photocatalytic efficiency observed could be due to the loss of TiO$_2$ nanoparticles during the washing of the films. Moreover, we demonstrate that the color of titanium dioxide does not change after several photocatalytic cycles, which confirms the preservation of the surface peroxo-titanium complexes and the fact that the material structure remains stable. XPS analysis was used to compare the oxygen groups before and after the reaction and the results (Fig. S14) revealed that the Ti^{4+} groups at 458.57 increased from 58.54% to 66.71% and the Ti(O) groups also increased slightly from 6.27, whereas the rest of the groups are represented by the Ti(B), which is due to charged groups. This shows that the materials have not changed significantly, but further systematic investigation is needed to establish the stability profile over varying reaction times.

The temperature stability of the peroxo-TiO$_2$ was also evaluated by comparing the crystal properties of the y-TiO$_2$ before and after treating at 550 °C and comparing the XRD spectra and the optical properties. The XRD spectra shows that only pure anatase forms were obtained and the broad peaks, which are typical of the peroxo-TiO$_2$ disappeared upon annealing. This could be due to the decomposition of the peroxo groups at high temperature coupled with the release of water and consequent reduction of the residual oxygen content, which is in line with the XPS results (Table S2). It is a well-known phenomenon that the heating of nanostructured materials causes changes in the morphology and crystal structure because of sintering and other reactions of the chemical groups. UV-vis spectra of the y-TiO$_2$ before and after annealing revealed significant changes as the annealed material showed a blue shift in the absorption spectra coupled with an increase in the bandgap from 2.40 to 3.14 (Fig. 9A and B). Thus, we confirmed that the yellow TiO$_2$ material is highly stable at room temperature in air atmosphere, but decomposition of the peroxo groups occurs when the material was annealed at 550 °C which is in line with previous studies.
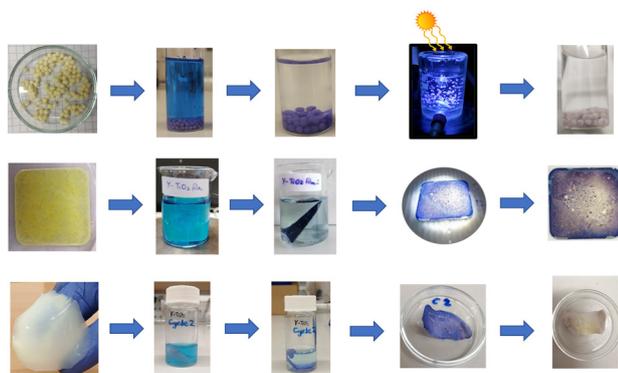

Fig. 6 Solar photocatalytic degradation of methylene blue dye adsorbed on y-TiO$_2$ deposited plate, beads and film for their recycling.
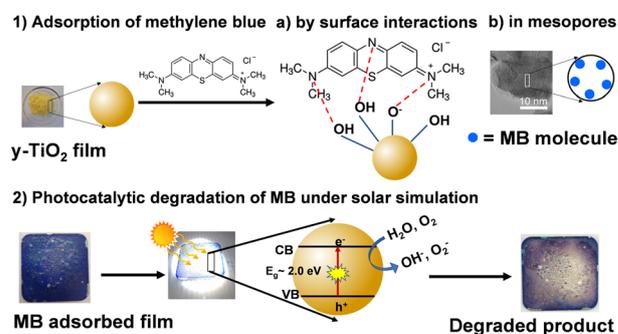

Fig. 7 Proposed mechanism of MB removal on y-TiO$_2$ through (1) adsorption and (2) photocatalytic degradation.
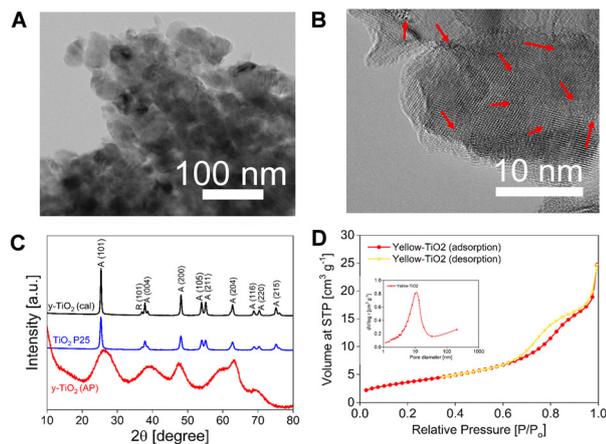
This journal is © The Royal Society of Chemistry 2025

Catal. Sci. Technol., 2025, 15, 5986–6000 | 5993

Fig. 8 (A) TEM and (B) HRTEM images of the y-TiO$_2$ catalysts with defects marked with red arrows. (C) XRD spectra of the synthesized materials and (D) N$_2$ adsorption–desorption isotherm (inset: pore size distribution of the y-TiO$_2$ catalysts).
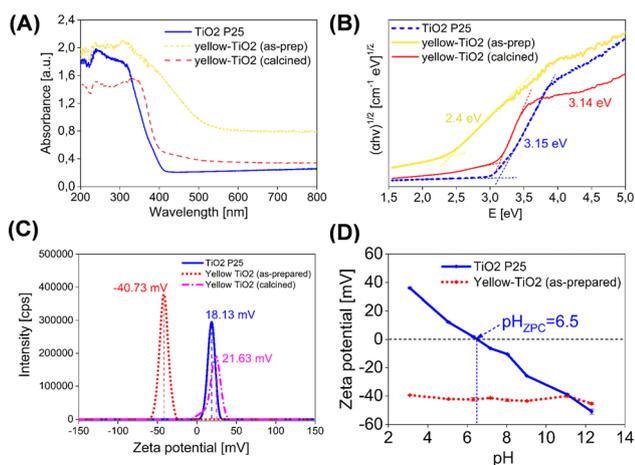

Fig. 9 (A) UV-vis absorption spectra of the catalysts. (B) Tauc plot of the optical bandgap energy calculated by extrapolation of the linear part of $(\alpha h\nu)^{1/2}$ versus (hc/λ) from UV-DRS measurements. (C) Zeta potential distribution of the catalysts. (D) Effect of solution pH on the zeta potential values of the catalysts.

Mechanism of photocatalytic degradation over y-TiO$_2$ catalyst

Based on the material surface and chemical properties and the kinetic measurements conducted, the dye removal is thought to occur in two steps: (1) adsorption in the dark and (2) photocatalytic degradation under solar-simulated irradiation. There are two probable mechanisms by which the adsorption of MB onto y-TiO$_2$ could occur. The first is by interactions between the dye and the adsorbent surface. The main surface interactions include electrostatic interactions between the highly negatively charged particle surface with a potential of −40.73 mV (Table S3) and the positively charged MB dye molecules. Another possible surface interaction is the hydrogen bonding interactions between the non-ionic parts of the dye and the reactive OH

groups on the nanoparticle surface (Fig. 7). After the calcination of the y-TiO$_2$, the charge on the surface changed from highly negative (−40.73 mV) to positive (+21.97 mV), which also corresponded to the loss in adsorption ability of the material towards methylene blue dye. It was confirmed by XPS that there was a reduction in the surface oxygen groups due to the re-oxidation of the y-TiO$_2$, thus resulting in a positive surface charge. Similarly, adsorption studies conducted at varying pH revealed low adsorption at low pH values with the adsorption increasing at increasing pH. This points to the fact that the presence of more H$^+$ ions compete with the MB dye cations for the active sites present on the adsorbent surface. The second phenomenon is physical adsorption due to the high surface area from the highly mesoporous structure, which accounts for the high dye adsorption (Table S3).

Thus, there is transfer of the dye from solution either onto the surface of the adsorbent or into the small pores. However, the fact that w-TiO$_2$ had a higher surface area than y-TiO$_2$ but with y-TiO$_2$ exhibiting higher adsorption capacity means the physical adsorption in pores is not the only phenomenon occurring. Similarly, the adsorption tests conducted at different pH values revealed that the adsorption did not improve much as the surface charge of TiO$_2$ P25 became more negative. This points to the fact that the high surface areas also contributed significantly to the high adsorption. The adsorption process is followed by the photocatalytic degradation of the dye under irradiation using a solar simulator where the dye is degraded to colourless products with the help of photogenerated active species. Thus, overall, the synergistic effects of adsorption and photocatalytic degradation could be responsible for the effective dye removal in such a short contact time (30–120 min).

Structure and properties of the y-TiO$_2$ catalysts

The structure and physicochemical properties of catalysts play a critical role in their overall catalytic performance. Thus, the developed y-TiO$_2$ photocatalysts were systematically characterized. The TEM images showed that the y-TiO$_2$ catalyst particles were aggregated (Fig. 8A) with amorphous regions interspersed with crystalline ones. From an enlarged image (Fig. 8B), the lattice fringe spacings are clearly visible, confirming the formation of crystalline TiO$_2$. XRD spectra (Fig. 8C) were employed to further confirm the presence of Ti in the structure of the as-prepared peroxo-TiO$_2$ (y-TiO$_2$ AP). The commercial TiO$_2$ P25 showed a highly crystalline structure with signature anatase (JCPDS no. 21-1272) and rutile anatase (JCPDS no. 21-1276) peaks. The spectra of the as-prepared y-TiO$_2$ on the other hand reveals peaks that match the anatase crystal form of titania, but the peaks were broad and slightly shifted when compared to those of the commercial TiO$_2$ P25. There was no additional peak detected in the spectrum of y-TiO$_2$. The fact that no distinct peak was observed, which corresponds to the peroxo groups, confirms

5994 | *Catal. Sci. Technol.*, 2025, **15**, 5986–6000

This journal is © The Royal Society of Chemistry 2025

the amorphous nature of the peroxo-TiO$_2$ complex, making the anatase peaks of the as-prepared material appear rather broad. As shown in Fig. 8D, the adsorption isotherm of y-TiO$_2$ particles combined with the pore size distribution (inset) obtained from N$_2$ adsorption isotherm measurements confirmed the highly mesoporous structure with high BET surface areas of >380 m^2 g^{-1}. The highly mesoporous structure is due to the stabilizer used during the synthesis (Table SI 1). These results are consistent with the TEM image which shows the highly mesoporous structure (Fig. 8B), with the observed surface area being several orders of magnitude higher than those of other TiO$_2$ materials reported previously with surface areas lower than 50 m^2 g^{-1}.[12]

Comparing the light absorption properties, y-TiO$_2$ showed a red-shift in the absorption spectrum (Fig. 9A), which suggests a lower bandgap energy. Our calculation of bandgaps from the Tauc plot based on the recommended approach confirmed that y-TiO$_2$ has a lower bandgap energy of 2.42 eV compared to that of the benchmark commercial TiO$_2$ P25 of 3.15 eV. This result also corresponded with the shift in the light absorption from the UV region into the visible region (Fig. 9A and B). This improved light absorption is of practical importance for sunlight-driven catalytic activity. After calcination of the y-TiO$_2$, there was a blue shift in the absorbance peak back to lower wavelengths, with a corresponding increase in the bandgap energy to 3.14 eV and a reduction in absorbance in the visible region.

To understand the dye adsorption behaviour and photocatalytic degradation, we investigated the surface charges of all the catalysts by zeta potential and XPS measurements. The surface of our as-synthesized peroxo-TiO$_2$ catalyst was found to be negatively charged, whereas that of the commercial TiO$_2$ P25 NPs was positively charged. Interestingly, the as-prepared y-TiO$_2$ surface carries a high negative surface charge of around −41 mV, whereas the surface charge changes to positive (+21 mV) after calcination, suggesting the loss of the surface groups (Fig. 9C, see also Table S4). The high negative charge on the as-prepared y-TiO$_2$ is permanent and does not change significantly with varying pH values of 3–11 as compared with TiO$_2$ P25, whose surface charges changed with changing pH (Fig. 9D). The stable negative surface charge is due to the abundant oxygen groups present on the surface of y-TiO$_2$ as revealed by XPS analysis of the as-synthesized yellow TiO$_2$ (Table S2). Unlike Ti^{4+}, which has an oxidation number of 4 making the molecule neutral, there is a reasonable amount of charged Ti groups (>40% of all Ti groups) on the surface, mainly due to the presence of negatively charged O groups.

The initial solution pH has been identified as one of the key parameters that affects the adsorbent surface charge and degree of ionization of the dye molecule in solution;[52,53] the influence of solution pH on the adsorption capacities was investigated. Results from adsorption tests conducted at different pH values revealed that for commercial TiO$_2$ P25,

the adsorption remained constant with changing pH until 9.0 despite the fact that the surface charge changed and became more negative from 36 mV at pH 3.04 to −51 mV at pH 11. Above pH 11, the adsorption began to increase slightly and this could be due to the effect of the high amount of base added to adjust the solution pH. This low adsorption efficiency, despite the high negative surface charge under basic conditions, points to the fact that the surface area plays a major role in the fast adsorption step, with electrostatic interactions playing a minimal role. Thus, the low surface area of P25 could not facilitate high adsorption.

In the case of y-TiO$_2$, it was observed that the adsorption efficiencies were lower at acidic pH, and increased with increasing solution pH, which corresponded to the fact that MB is a cationic species and is readily adsorbed on materials/surfaces with more negative charges. Despite the fact that the surface charge of the y-TiO$_2$ remained unchanged in the entire pH range (Fig. 9D), the adsorption capacity increased as the pH increased from 3 to 8, reaching a full removal efficiency of 100% at around pH 7.18 (Fig. SI8a). This indicates that despite the fact that the adsorbent surface zeta potential does not significantly change, the methylene blue structure is protonated or deprotonated at different pH values and this accounts for the differences in adsorption at different pH values. This is in line with previous reports that the pH has an effect on the chemical structure of the dye in solution.[54] For instance, during a MB degradation test, Nawaz and coworkers observed an increased degradation rate between pH 3 to 7 with the highest degradation achieved at pH 7. Further increase in the pH beyond 8 resulted in a decrease in the degradation rate.[55]

From Fig. S8 in the SI, it was observed that at lower pH values, the electrostatic interaction between the negatively charged y-TiO$_2$ and the positively charged MB dye was less due to the presence of H$^+$ ions, which compete for the same binding sites on the surface of the adsorbent.[56] Moreover, the protonation of the N$^+$ and S$^+$ groups on MB at low pH values, which reduces the amount of positive charges, could lead to repulsion between the neutral MB dye and the negatively charged y-TiO$_2$ surface. Beyond pH values higher than 7.0, the adsorption capacity decreased again. This could be due to the fact that the presence of excess OH$^-$ groups in solution could compete with the negatively charged particle surface for the binding to the positively charged dye, thus the lower adsorption. Therefore, subsequent adsorption tests were carried out in the pH range 6 to 7 for optimal interaction between the MB dye and the y-TiO$_2$ particles. These results combined with the surface area measurements further confirmed that for y-TiO$_2$, the adsorption is not only due to electrostatic interactions occurring on the surface but also other phenomena such as physical adsorption in the small pores of the highly mesoporous y-TiO$_2$. If the adsorption process was solely controlled by the surface charges, it would be expected that the y-TiO$_2$ material adsorbs more or less the same amount of MB in the entire pH range as the surface charge did not change significantly.

This journal is © The Royal Society of Chemistry 2025

Catal. Sci. Technol., 2025, 15, 5986–6000 | 5995

However, it was evident that the adsorption was mainly based on a combination of physical adsorption in the small pores, electrostatic interactions and hydrogen bonding due to the surface charges.

Surface chemical species and the role of PVA or PVP in stabilizing defects

XPS results revealed the surface composition of the y-TiO$_2$ materials consisting of three main elements C, Ti, and O with photoelectron peaks corresponding to C 1s, Ti 2p and O 1s, respectively (Fig. S9a). The as-prepared y-TiO$_2$ showed a 23% higher oxygen content compared to the commercial TiO$_2$ P25, which confirms the formation of peroxo groups (Table S2). Two major components C=C (284.4 ± 0.4 eV) and C–C (285.0 ± 0.4 eV) with sp^2 and sp^3 hybridization, respectively, were determined on the C 1s orbital. The functional groups C–O (286.3 ± 0.4 eV), C=O (288 ± 0.4 eV) and O–C=O (289.0 ± 0.4 eV) were also represented to a lesser extent. The carbon detected in the titanium samples can be due to adventitious carbon and thus not considered in detail. The O 1s orbital was dominated by the two main components TiO$_2$ (529.7 ± 0.4) and TiO$_2$ (531.0 ± 0.4 eV),[57] where O was organic. Furthermore, the functional groups C–O (532.6 ± 0.4 eV), C=O (531.3 ± 0.4), O–C=(O) (531.6 ± 0.4 eV, (O) was aromatic) and O–C=O (533.2 ± 0.4) were determined on the O 1s orbital (Table S2). In fact, the as-synthesized y-TiO$_2$ has a higher amount of oxygen with an O/Ti ratio of 4 as compared to the other materials which had ratios ranging between 2.6 and 3.4. The O groups were mainly from Ti–O, Ti–OH, –C–O– and O(B). The O(B) groups were attributed to surface charging (Table S2).

We discovered that the yellow-coloured, as-synthesized, y-TiO$_2$ comprises four different Ti valence states (Fig. 10A and B), signifying the presence of defects which were stabilized due to the presence of polymeric stabilizers in the reaction medium. The amount of Ti^{4+} in the as-prepared y-TiO$_2$ is only 58.54% compared to that of the commercial TiO$_2$ (100%) and the white mesoporous TiO$_2$ (93.47%), prepared without H$_2$O$_2$. The lower amount of Ti^{4+} and the presence of other Ti valence states in y-TiO$_2$ is probably due to the presence of the polymeric stabilizer, which interferes with the formation of the pure TiO$_2$ phase and causes the reduction of Ti^{4+} to Ti^{3+} and Ti^{2+}. Similar results were reported in the case of coloured TiO$_2$ and TiO$_2$–SiO$_2$ composites.[37,38]

The FTIR spectra of the as-prepared y-TiO$_2$ measured 3 years apart (see Fig. S10) revealed that the two spectra were similar, implying that the y-TiO$_2$ catalyst was very stable during the storage time (of more than 3 years). When the y-TiO$_2$ powder was calcined at 550 °C, a light yellow product was obtained, which was accompanied by a significant reduction in the Ti^{2+} species from 11.76 wt% to 2.55 wt%, whereas the Ti^{3+} increased from 20.24 wt% to 33.45 wt% (Fig. 9C and D). This increase in the Ti^{3+} content is due to the oxidization of the lower oxidation state groups during the calcination process.

To investigate the role of Ti^{3+} and other defects on extending the light absorption of TiO$_2$, a new mesoporous TiO$_2$ was synthesized but without addition of H$_2$O$_2$, which resulted in a white mesoporous TiO$_2$ with only two Ti valence states, Ti^{4+} and Ti^{3+} (see Fig. S11c), as compared to the as-prepared y-TiO$_2$ with four different Ti states. This material was labelled w-TiO$_2$ because of its white colour similar to that of commercial TiO$_2$ P25 with only one valence state of Ti (see Fig. S11d). Evaluating the effect of the various defects on the colour of the materials, it was obvious that the presence of Ti^{3+} was not responsible for the deep bright yellow colour of the y-TiO$_2$ materials. If this was the case, the calcined material (Fig. 10B), which had a higher amount of Ti^{3+} compared to the as-prepared y-TiO$_2$ (Fig. 10A), will be expected to have a deeper yellow colour. Moreover, the as-prepared w-TiO$_2$, which also had about 6.5 wt% Ti^{3+}, showed a white colour with no traces of yellow. This indicates that Ti^{2+}, rather than Ti^{3+}, might be responsible for the yellow colour. This postulation was further confirmed by the fact that after the calcination of y-TiO$_2$, the amount of Ti^{2+} reduced from 11.8% to 2.6%, which also corresponded to a reduction in the colour to a pale yellow colour (Fig. 10D).

Similar results have been reported previously where the authors observed that Ti^{3+} was not responsible for the obvious yellow colour, but rather the creation of other defects or external dopants, although the authors did not clearly specify which other defects were responsible for the yellow colour.[18] Nevertheless, a number of studies have demonstrated that reduced TiO$_2$ containing Ti^{3+} or oxygen vacancies exhibits visible light absorption.[29]

To confirm the unique role of the polymeric stabilizers in the formation of the stable peroxo-TiO$_2$, we synthesized a mesoporous TiO$_2$ with H$_2$O$_2$ alone, but without adding any water-soluble stabilizer (neither PVA nor PVP). We found that
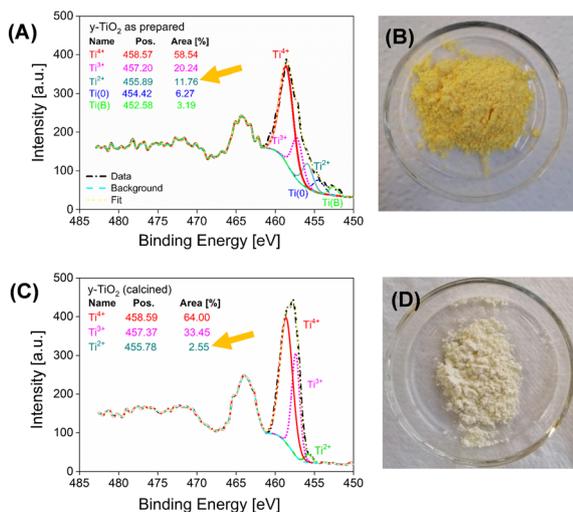

Fig. 10 XPS surface composition showing the different Ti valence states and photos of y-TiO$_2$. (A and B) As-prepared y-TiO$_2$ and (C and D) calcined y-TiO$_2$.

the yellow colour of y-TiO$_2$ was formed initially when hydrogen peroxide was added to the reaction mixture, but it soon disappeared before the end of the reaction (see Fig. S12b). This points to the fact that the defects created in the material, which led to the production of the yellow colour, were only short-lived and quickly re-oxidized back to Ti^{4+} by the time the reaction was over. Conversely, the peroxo-TiO$_2$ synthesized using polymeric stabilizers, e.g. PVA, remained stable. Based on these results, a possible mechanism for the role of PVA in stabilizing the defects was suggested. It has been previously reported that the oxidation of PVA using H$_2$O$_2$ results in an increase in carbonyl and carboxyl groups, even though the mechanism is not completely understood.[58] Thus, we were interested in understanding whether the reaction between PVA and H$_2$O$_2$ in the presence of the TTIP precursor led to the oxidation of PVA by H$_2$O$_2$ to form stable Ti–O and Ti–OH bonds and –CO– groups, which may be the reason for the long-term stability. This was confirmed by XPS analysis where all these groups were present in the as-prepared y-TiO$_2$. Interestingly, the stable yellow colour of the as-prepared y-TiO$_2$ was retained for longer than 3 years (Fig. 1 and S10 in the SI), confirming the difference between y-TiO$_2$ and the extensively studied titanium superoxide.[59–61] In general, the formed surface groups should be stable under normal laboratory or environmental conditions. However, we noticed that upon calcination treatments in air, most of these charged functional groups were oxidized (Table S2 in the SI).

To further demonstrate the existence of defects in y-TiO$_2$, continuous wave electron paramagnetic resonance (cw-EPR) measurements were conducted for y-TiO$_2$ samples before and after calcination and compared with the commercial TiO$_2$ P25 (Fig. 11). The P25 reference does not show any strong signals in the cw-EPR measurements, but due to the very
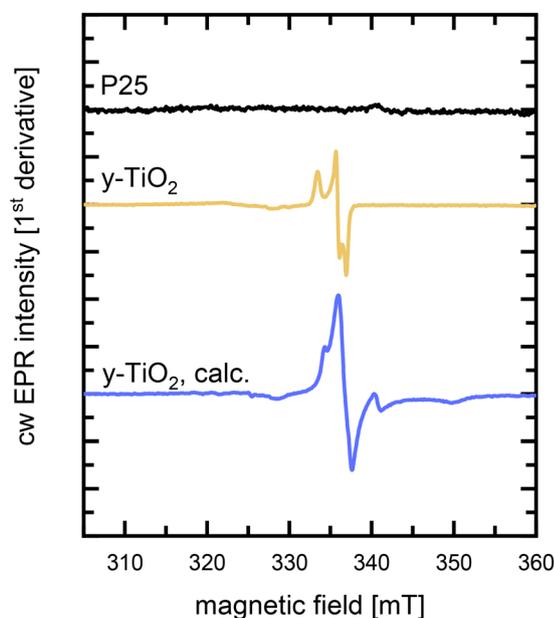
weak peak around $g \approx 1.98$ the presence of some Ti^{3+} cannot be fully excluded from these measurements. The y-TiO$_2$ sample exhibits signals which can be attributed to O$_2^-$ species (g_{zz} = 2.0248, g_{yy} = 2.0096, g_{xx} = 2.0038)[62] and are presumably due to oxidation with H$_2$O$_2$. Additionally, weak signals at lower magnetic field are presumably due to a Cu^{2+} impurity.[63] For this sample, no indication for EPR-active Ti^{3+} species is found. Yet, a notably lowered Q-factor, as compared to the other samples, indicates an increased conductivity and thus the presence of defects with delocalized electrons, which escape EPR-detection. For the calcined y-TiO$_2$ sample, the EPR spectrum is dominated by a signal around g = 2.005 which is assigned to paramagnetic carbon species.[64] The small signal around g = 2.02 may indicate that some O$_2$-species remain present on the surface also after calcination. Yet, the signal is largely obscured by the strong signal at g = 2.005 and clearly their intensity is significantly reduced as compared to the sample before calcination, suggesting decomposition of these species during calcination. Similar to the sample before calcination, weak signals at lower magnetic fields are tentatively attributed to a Cu^{2+} impurity. Furthermore, the calcined y-TiO$_2$ sample exhibits signals which can be attributed to Ti^{3+} ($g_\perp$ = 1.98, $g_\parallel$ = 1.93).[65] The detection of Ti^{3+} after calcination of y-TiO$_2$ is consistent with the XPS results.

Fig. 11 cw-EPR measurements of different TiO$_2$ samples (110 K). The spectra were shifted for improved visibility.

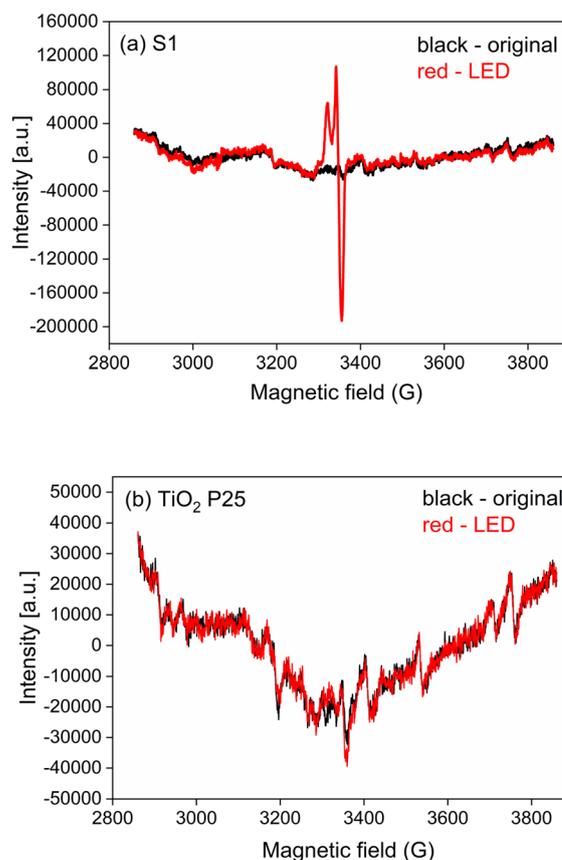**Fig. 12** EPR spectra of (a) S1 – yellow TiO$_2$ synthesized with PVP as a stabilizer, and (b) white commercial TiO$_2$ P25.

This journal is © The Royal Society of Chemistry 2025

Catal. Sci. Technol., 2025, **15**, 5986–6000 | **5997**

To investigate photoinduced effects due to the presence of defects, four samples were studied using electron paramagnetic resonance (EPR) spectroscopy: S1, S2, S3, and P25. These samples were synthesized with or without stabilizers to yield different colored powders (yellow color due to the presence of defects and white color for those without defects). EPR measurements were performed at room temperature. Illumination was carried out using a white LED light source with a broad spectral range spanning approximately from 450 to 650 nm. The samples were exposed to light for one minute prior to the start of spectrum acquisition, and illumination continued during the magnetic field sweep. Following the illumination phase, the samples were kept in the dark for 5 minutes, after which a new spectrum was recorded. A noticeable decrease in signal intensity was observed, indicating relaxation of photoinduced states. Complete relaxation takes approximately 1 h, as shown in the RT graph. The results of the photoinduced analysis (Fig. 12) revealed a pronounced photoresponse in samples S1 and S3, which were both prepared using stabilizers and had a deep yellow colour, whereas samples S2 and S4 exhibited either no significant photoeffect or a very weak one and this also corresponds with their white colour.

Photoelectrochemical experiments were also performed to investigate the photoinduced electron transfer processes in the developed y-TiO$_2$. As shown in Fig. 13, the response to visible light could be seen during on–off cycles of solar simulator irradiation with the photocurrent density of y-TiO$_2$ and calcined y-TiO$_2$ being 19 and 30 μA cm^{-2}, respectively. Upon calcination at 550 °C, the photocurrent density of the calcined material was higher than that of the as-prepared material, confirming that its separation efficiency of the photogenerated charge carriers was higher under similar experimental conditions. Thus, these results confirm y-TiO$_2$'s response to light and the efficiency of the charge carrier separation.
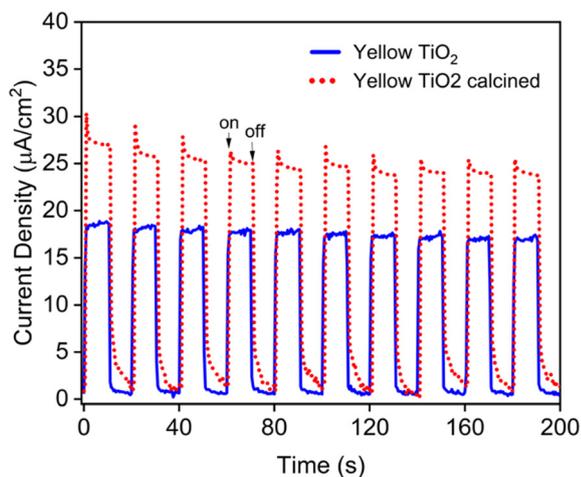

Fig. 13 Transient photocurrent–time profiles of yellow TiO$_2$ before and after calcination under solar simulator irradiation.

Overall, this simple and new approach offers new options for the development of stable, defect-rich titania materials, which are relevant for sunlight-driven research and industrial applications.

Conclusions

We have successfully synthesized a highly stable, defect-rich peroxo-TiO$_2$ with high photocatalytic activity by a simple approach, which combines sol–gel and colloidal methods using polymeric stabilizers to stabilize the defects. The highly mesoporous material possesses four different titanium states (i.e. Ti^{4+}, Ti^{3+}, Ti^{2+} and Ti^0), a low bandgap of 2.0 eV, high surface area >380 m^2 g^{-1} and solar-simulated photocatalytic activity. The high photocatalytic activity in hydrogen production and model pollutant degradation were attributed to the improved light absorption, high surface area and presence of defects. Our results also revealed that the Ti^{3+} species were not responsible for the deep yellow colour of yellow TiO$_2$, but rather Ti^{2+} and other species. The presented results indicate that the y-TiO$_2$ developed in this study enhanced light absorption and adsorption, and the stabilized defects in the material led to an overall long-term stability of the catalyst and ultimately enhanced the photocatalytic performance. The new synthetic approach, which is simple and robust, will be explored for the development of other stable, defect-rich solar-sensitive photocatalysts with improved performance for various applications.

Author contributions

Edith Mawunya Kutorglo: conceptualization, investigation, methodology, project administration, funding acquisition, investigation, formal analysis, writing – original draft, writing – review & editing. Jan Šmahlík: investigation, validation, visualization, writing – review & editing. Yusef Hassana: investigation, validation, visualization, writing – review & editing. Minoo Tasbihi: investigation, validation, writing – review & editing. Pavel Sialini: investigation, validation, writing – review & editing. Wiebke Riedel: investigation, validation, writing – review & editing. Andrey Prokhorov: methodology, investigation, validation, writing – review & editing. Eliška Zmeškalová: methodology, investigation, validation, writing – review & editing. Kousik Das: methodology, investigation, validation, writing – review & editing. Reinhard Schomäcker: supervision, resources, funding acquisition, writing – review & editing. Miroslav Šoóš: supervision, funding acquisition, resources, writing – review & editing. Michael Schwarze: supervision, resources, investigation, methodology, validation, visualization, funding acquisition, writing – review & editing.

Conflicts of interest

There are no conflicts to declare.

5998 | Catal. Sci. Technol., 2025, 15, 5986–6000

This journal is © The Royal Society of Chemistry 2025

Data availability

Supplementary information available: A description of the materials and instruments, preparation of white, mesoporous-TiO_2 particles (w-TiO_2 NPs), catalyst physicochemical characterization, adsorption-degradation tests and adsorption mechanisms and results. Tables summarizing the textural properties, surface charges and adsorption behaviour of the materials. Electrophoretic mobility of the particles in μmcm/Vs and conductivity. See DOI: https://doi.org/10.1039/D4CY00724G.

The data supporting this article have been included as part of the SI.

Acknowledgements

References

1 A. Gil, A. M. García, M. Fernández, M. A. Vicente, B. González-Rodríguez, V. Rives and S. A. Korili, *J. Ind. Eng. Chem.*, 2017, **53**, 183–191.

2 Y. Lin, Y. Liu, Y. Li, Y. Cao, J. Huang, H. Wang, H. Yu, H. Liang and F. Peng, *ACS Sustainable Chem. Eng.*, 2018, **6**, 17340–17351.

3 K. Umar, A. Aris, H. Ahmad, T. Parveen, J. Jaafar, Z. A. Majid, A. V. B. Reddy and J. Talib, *J. Anal. Sci. Technol.*, 2016, **7**, 29.

4 X. Fang, X. Huang, Q. Hu, B. Li, C. Hu, B. Ma and Y. Ding, *Chem. Commun.*, 2024, **60**, 5354–5368.

5 C. Gu, T. Yatabe, K. Yamaguchi and K. Suzuki, *Chem. Commun.*, 2024, **60**, 4906–4909.

6 H. Idriss, *Catal. Sci. Technol.*, 2020, **10**, 304–310.

7 S. Bai, N. Zhang, C. Gao and Y. Xiong, *Nano Energy*, 2018, **53**, 296–336.

8 E. M. Jubeer, M. A. Manthrammel, P. A. Subha, M. Shkir, K. P. Biju and S. A. AlFaify, *Sci. Rep.*, 2023, **13**, 16820.

9 D. Maarisetty and S. S. Baral, *J. Mater. Chem. A*, 2020, **8**, 18560–18604.

10 J. Li and N. Wu, *Catal. Sci. Technol.*, 2015, **5**, 1360–1384.

11 K. Rajeshwar, A. Thomas and C. Janaky, *J. Phys. Chem. Lett.*, 2015, **6**, 139–147.

12 F. Zuo, K. Bozhilov, R. J. Dillon, L. Wang, P. Smith, X. Zhao, C. Bardeen and P. Feng, *Angew. Chem., Int. Ed. Engl.*, 2012, **51**, 6223–6226.

13 Y. Huang, L. Meng, W. Xu and L. Li, *Adv. Funct. Mater.*, 2023, **33**, 2305940.

14 X. Tao, X. Zhou and R. Li, *Chem. Commun.*, 2024, **60**, 5136–5148.

15 M. T. Uddin, Y. Nicolas, C. Olivier, W. Jaegermann, N. Rockstroh, H. Junge and T. Toupance, *Phys. Chem. Chem. Phys.*, 2017, **19**, 19279–19288.

16 B. J. Morgan and G. W. Watson, Intrinsic n-type defect formation in TiO_2: A Comparison of rutile and anatase from GGA+U Calculations, *J. Phys. Chem. C*, 2010, **114**, 2321–2328.

17 Y. Li, Y.-L. Li, B. Sa and R. Ahuja, *Catal. Sci. Technol.*, 2017, **7**, 545–559.

18 Q. Wu, F. Huang, M. Zhao, J. Xu, J. Zhou and Y. Wang, *Nano Energy*, 2016, **24**, 63–71.

19 L. Sun, W. Liu, R. Wu, Y. Cui, Y. Zhang, Y. Du, S. Liu, S. Liu and H. Wang, *Nanoscale*, 2020, **12**, 746–754.

20 C. Fan, C. Chen, J. Wang, X. Fu, Z. Ren, G. Qian and Z. Wang, *Sci. Rep.*, 2015, **5**, 11712.

21 X. Xin, T. Xu, J. Yin, L. Wang and C. Wang, *Appl. Catal., B*, 2015, **176-177**, 354–362.

22 M. Bellardita, C. Garlisi, L. Y. Ozer, A. M. Venezia, J. Sá, F. Mamedov, L. Palmisano and G. Palmisano, *Appl. Surf. Sci.*, 2020, **510**, 145419.

23 S. Sorcar, Y. Hwang, J. Lee, H. Kim, K. M. Grimes, C. A. Grimes, J.-W. Jung, C.-H. Cho, T. Majima, M. R. Hoffmann and S. I. In, *Energy Environ. Sci.*, 2019, **12**, 2685–2696.

24 S. Sorcar, J. Thompson, Y. Hwang, Y. H. Park, T. Majima, C. A. Grimes and J. R. Durrant, *Energy Environ. Sci.*, 2018, **11**, 3183–3193.

25 N. L. De Silva, A. C. A. Jayasundera, A. Folger, O. Kasian, S. Zhang, C.-F. Yan, C. Scheu and J. Bandara, *Catal. Sci. Technol.*, 2018, **8**, 4657–4664.

26 W. K. Jo and H. J. Yoo, *Ultrason. Sonochem.*, 2018, **42**, 517–525.

27 S. Tan, Z. Xing, J. Zhang, Z. Li, X. Wu, J. Cui, J. Kuang, Q. Zhu and W. Zhou, *J. Catal.*, 2018, **357**, 90–99.

28 S. G. Ullattil, S. B. Narendranath, S. C. Pillai and P. Periyat, *Chem. Eng. J.*, 2018, **343**, 708–736.

29 F. Zuo, L. Wang, T. Wu, Z. Zhang, D. Borchardt and P. Feng, *JACS Communications*, 2010, **132**, 11856.

30 C. Mao, F. Zuo, Y. Hou, X. Bu and P. Feng, *Angew. Chem., Int. Ed. Engl.*, 2014, **53**(39), 10485.

31 X. Bi, G. Du, D. Sun, M. Zhang, Y. Yu, Q. Su, S. Ding and B. Xu, *Appl. Surf. Sci.*, 2020, **511**, 145617.

32 F. Liu, Y. H. Leung, A. B. Djurišić, A. M. C. Ng and W. K. Chan, *J. Phys. Chem. C*, 2013, **117**, 12218–12228.

33 M. T. Dehghani and M. Delnavaz, *Sci. Rep.*, 2024, **14**(1), 5195.

34 M. Wisniewska, I. Ostolska, K. Szewczuk-Karpisz, S. Chibowski, K. Terpilowski, V. M. Gun'ko and V. I. Zarko, *J. Nanopart. Res.*, 2015, **17**(1), 12.

This journal is © The Royal Society of Chemistry 2025

Catal. Sci. Technol., 2025, **15**, 5986–6000 | **5999**

35 A. V. Nimmy, V. M. Anandakumar and V. Biju, *Discover Mater.*, 2025, **5**, 45.

36 X. Li, C. Chen and J. Zhao, *Langmuir*, 2001, **17**, 4118.

37 Y. Nosaka and A. Nosaka, *ACS Energy Lett.*, 2016, **1**(2), 356.

38 V. D. Chinh, A. Broggi, L. Di Palma, M. Scarsella, G. Speranza, G. Vilardi and P. N. Thang, *J. Electron. Mater.*, 2017, **47**(4), 2215.

39 K. Maeda, *Catal. Sci. Technol.*, 2014, **4**, 1949–1953.

40 S. Bashir and H. Idriss, *Catal. Sci. Technol.*, 2017, **7**, 5301–5320.

41 D. P. Serrano, G. Calleja, P. Pizarro and P. Gálvez, *Int. J. Hydrogen Energy*, 2014, **39**, 4812–4819.

42 Y. Ma, Y. Ma, T. Lv, X. Deng, X. Kuang, J. Zhang, Q. Liu and Y. Zhang, *Catal. Sci. Technol.*, 2022, **12**, 3856–3862.

43 G. Nagaraju, K. Manjunath, S. Sarkar, E. Gunter, S. R. Teixeira and J. Dupont, *Int. J. Hydrogen Energy*, 2015, **40**, 12209–12216.

44 S. K. Parayil, R. J. Psota and R. T. Koodali, *Int. J. Hydrogen Energy*, 2013, **38**, 10215–10225.

45 T. J. Wong, F. J. Lim, M. Gao, G. H. Lee and G. W. Ho, *Catal. Sci. Technol.*, 2013, **3**, 1086.

46 Y. Chen and Z. Qin, *Catal. Sci. Technol.*, 2016, **6**, 8212–8221.

47 Y. Zhou, H. Qin, S. Fang, Y. Wang, J. Li, G. Mele and C. Wang, *Catal. Sci. Technol.*, 2022, **12**, 7151–7160.

48 E. Pulido Melián, M. Nereida Suárez, T. Jardiel, D. G. Calatayud, A. del Campo, J. M. Doña-Rodríguez, J. Araña and O. M. González Díaz, *Int. J. Hydrogen Energy*, 2019, **44**, 24653–24666.

49 C.-C. Lin, T.-Y. Wei, K.-T. Lee and S.-Y. Lu, *J. Mater. Chem.*, 2011, **21**, 12668.

50 Z. Pei, S. Weng and P. Liu, *Appl. Catal., B*, 2016, **180**, 463–470.

51 J. Yan, L. Dai, P. Shi, J. Fan, Y. Min and Q. Xu, *CrystEngComm*, 2020, **22**, 4030–4038.

52 C. Leodopoulos, D. Doulia and K. Gimouhopoulos, *Sep. Purif. Technol.*, 2014, **44**, 74–107.

53 H. Liu, W. Guo, Y. Li, S. He and C. He, *J. Environ. Chem. Eng.*, 2018, **6**, 59–67.

54 X. Zhao, X. Wang and T. Lou, *J. Hazard. Mater.*, 2021, **403**, 124054.

55 A. Nawaz, A. Khan, N. Ali, N. Ali and M. Bilal, *Environ. Technol. Innovation*, 2020, **20**, 101079.

56 C. Liu, A. M. Omer and X. K. Ouyang, *Int. J. Biol. Macromol.*, 2018, **106**, 823–833.

57 M. C. Biesinger, L. W. M. Lau, A. R. Gerson and R. S. C. Smart, *Appl. Surf. Sci.*, 2010, **257**, 887–898.

58 Y. Lu, Q.-M. Kong, R. Jing, X. Hu and P.-X. Zhu, *Polym. Degrad. Stab.*, 2013, **98**, 1103–1109.

59 R. Santhosh Reddy, T. M. Shaikh, V. Rawat, P. U. Karabal, G. Dewkar, G. Suryavanshi and A. Sudalai, *Catal. Surv. Asia*, 2010, **14**, 21–32.

60 G. Zhang, F. Fan, X. Li, J. Qi and Y. Chen, *Chem. Eng. J.*, 2018, **331**, 471–479.

61 X.-g. Zhao, J.-g. Huang, B. Wang, Q. Bi, L.-l. Dong and X.-j. Liu, *Appl. Surf. Sci.*, 2014, **292**, 576–582.

62 T. Berger, M. Sterrer, O. Diwald and E. Knozinger, *ChemPhysChem*, 2005, **6**(10), 2104.

63 G. Cordoba, M. Viniegra, J. L. G. Fierro, J. Padilla and R. Arroyo, *J. Solid State Chem.*, 1998, **138**, 1.

64 M. J. Elser, E. Neige, T. Berger, M. Chiesa, E. Giamello, K. McKenna, T. Risse and O. Diwald, *J. Phys. Chem. C Nanomater. Interfaces.*, 2023, **127**(18), 8778.

65 S. Livraghi, S. Maurelli, M. C. Paganini, M. Chiesa and E. Giamello, *Angew. Chem., Int. Ed.*, 2011, **50**(35), 8038.

6000 | *Catal. Sci. Technol.*, 2025, **15**, 5986–6000

This journal is © The Royal Society of Chemistry 2025